

Mass Production of 2023 KMTNet Microlensing Planets. II: Two Planets and A Brown Dwarf

ZHIXING LI,¹ HONGYU LI,^{2,1} WEICHENG ZANG,¹ YOON-HYUN RYU,³ ANDRZEJ UDALSKI,⁴ TAKAHIRO SUMI,⁵ HONGJING YANG,¹
YUCHEN TANG,¹ JIYUAN ZHANG,² AND SHUDE MAO¹
(LEADING AUTHORS)

MICHAEL D. ALBROW,⁶ SUN-JU CHUNG,³ ANDREW GOULD,^{7,8} CHEONGHO HAN,⁹ KYU-HA HWANG,³ YOUN KIL JUNG,^{3,10}
IN-GU SHIN,¹ YOSSI SHVARTZVALD,¹¹ JENNIFER C. YEE,¹² SANG-MOK CHA,^{3,13} DONG-JIN KIM,³ SEUNG-LEE KIM,³
CHUNG-UK LEE,³ DONG-JOO LEE,³ YONGSEOK LEE,^{3,13} BYEONG-GON PARK,³ AND RICHARD W. POGGE^{14,15}
(THE KMTNET COLLABORATION)

PRZEMEK MRÓZ,⁴ MICHAŁ K. SZYMAŃSKI,⁴ JAN SKOWRON,⁴ RADOSŁAW POLESKI,⁴ IGOR SOSZYŃSKI,⁴ PAWEŁ PIETRUKOWICZ,⁴
SZYMON KOZŁOWSKI,⁴ KRZYSZTOF A. RYBICKI,^{4,16} PATRYK IWANEK,⁴ KRZYSZTOF ULACZYK,¹⁷ MARCIN WRONA,^{4,18}
MARIUSZ GROMADZKI,⁴ AND MATEUSZ J. MRÓZ⁴
(THE OGLE COLLABORATION)

FUMIO ABE,¹⁹ KEN BANDO,⁵ DAVID P. BENNETT,^{20,21} APARNA BHATTACHARYA,^{20,21} IAN A. BOND,²² AKIHIKO FUKUI,^{23,24}
RYUSEI HAMADA,⁵ SHUNYA HAMADA,⁵ NAOTO HAMASAKI,⁵ YUKI HIRAO,⁵ STELA ISHITANI SILVA,^{25,20} NAOKI KOSHIMOTO,²¹
YUTAKA MATSUBARA,¹⁹ SHOTA MIYAZAKI,⁵ YASUSHI MURAKI,¹⁹ TUTUMI NAGAI,¹⁹ KANSUKE NUNOTA,¹⁹ GREG OLMSCHENK,²⁰
CLÉMENT RANC,²⁶ NICHOLAS J. RATTENBURY,²⁷ YUKI SATOH,⁵ DAISUKE SUZUKI,⁵ SEAN TERRY,^{20,21} PAUL J. TRISTRAM,²⁸
AIKATERINI VANDOROU,^{20,21} AND HIBIKI YAMA⁵
(THE MOA COLLABORATION)

¹Department of Astronomy, Westlake University, Hangzhou 310030, Zhejiang Province, China

²Department of Astronomy, Tsinghua University, Beijing 100084, China

³Korea Astronomy and Space Science Institute, Daejeon 34055, Republic of Korea

⁴Astronomical Observatory, University of Warsaw, Al. Ujazdowskie 4, 00-478 Warszawa, Poland

⁵Department of Earth and Space Science, Graduate School of Science, Osaka University, Toyonaka, Osaka 560-0043, Japan

⁶University of Canterbury, School of Physical and Chemical Sciences, Private Bag 4800, Christchurch 8020, New Zealand

⁷Max-Planck-Institute for Astronomy, Königstuhl 17, 69117 Heidelberg, Germany

⁸Department of Astronomy, Ohio State University, 140 W. 18th Ave., Columbus, OH 43210, USA

⁹Department of Physics, Chungbuk National University, Cheongju 28644, Republic of Korea

¹⁰National University of Science and Technology (UST), Daejeon 34113, Republic of Korea

¹¹Department of Particle Physics and Astrophysics, Weizmann Institute of Science, Rehovot 7610001, Israel

¹²Center for Astrophysics | Harvard & Smithsonian, 60 Garden St., Cambridge, MA 02138, USA

¹³School of Space Research, Kyung Hee University, Yongin, Gyeonggi 17104, Republic of Korea

¹⁴Department of Astronomy, Ohio State University, 140 West 18th Ave., Columbus, OH 43210, USA

¹⁵Center for Cosmology and AstroParticle Physics, Ohio State University, 191 West Woodruff Ave., Columbus, OH 43210, USA

¹⁶Department of Particle Physics and Astrophysics, Weizmann Institute of Science, Rehovot 76100, Israel

¹⁷Department of Physics, University of Warwick, Gibbet Hill Road, Coventry, CV4 7AL, UK

¹⁸Villanova University, Department of Astrophysics and Planetary Sciences, 800 Lancaster Ave., Villanova, PA 19085, USA

¹⁹Institute for Space-Earth Environmental Research, Nagoya University, Nagoya 464-8601, Japan

²⁰Code 667, NASA Goddard Space Flight Center, Greenbelt, MD 20771, USA

²¹Department of Astronomy, University of Maryland, College Park, MD 20742, USA

²²Institute of Natural and Mathematical Sciences, Massey University, Auckland 0745, New Zealand

²³Department of Earth and Planetary Science, Graduate School of Science, The University of Tokyo, 7-3-1 Hongo, Bunkyo-ku, Tokyo 113-0033, Japan

²⁴Instituto de Astrofísica de Canarias, Vía Láctea s/n, E-38205 La Laguna, Tenerife, Spain

²⁵Department of Physics, The Catholic University of America, Washington, DC 20064, USA

²⁶Sorbonne Université, CNRS, Institut d'Astrophysique de Paris, IAP, F-75014, Paris, France

²⁷Department of Physics, University of Auckland, Private Bag 92019, Auckland, New Zealand

²⁸University of Canterbury Mt. John Observatory, P.O. Box 56, Lake Tekapo 8770, New Zealand

ABSTRACT

To expand the homogeneous microlensing planetary sample of the Korea Microlensing Telescope Network (KMTNet), we investigate six planetary candidates identified by the AnomalyFinder search in the 2023 prime-field data, namely KMT-2023-BLG-1592, OGLE-2023-BLG-0766, KMT-2023-BLG-0332, KMT-2023-BLG-0486, KMT-2023-BLG-0792, and OGLE-2023-BLG-1043. Light-curve modeling indicates that the first two events have planetary mass ratios of $\log q \sim -3.0$ and -2.6 , while the third exhibits a brown dwarf mass ratio of $\log q \sim -1.4$. The remaining three events show the well-known degeneracy between the binary-lens single-source (2L1S) and single-lens binary-source (1L2S) interpretations. A Bayesian analysis yields companion masses of about 0.6 and 1.2 Jupiter masses for the two planetary systems, likely orbiting beyond the snow lines of M- or K-dwarf hosts. A review of the KMTNet planetary sample shows that candidates discovered by AnomalyFinder are significantly more likely to exhibit the 2L1S/1L2S degeneracy, consistent with the tendency of AnomalyFinder to detect subtler planetary signals.

1. INTRODUCTION

Microlensing offers a uniquely powerful and complementary pathway to exoplanet discovery (Mao & Paczynski 1991; Gould & Loeb 1992). In contrast to the transit and radial-velocity methods, which account for the vast majority of known planets, microlensing is intrinsically sensitive to cold planets at or beyond Jupiter-like separations across the full range of planetary masses, and even to unbound planetary-mass objects (Sumi et al. 2011; Mróz et al. 2017; Gould et al. 2022a; Sumi et al. 2023). Because the microlensing signal is independent of light from the host star, it enables the detection of planets orbiting faint or dark hosts, including brown dwarfs (e.g., Han et al. 2013) and white dwarfs (Blackman et al. 2021; Zhang et al. 2024), as well as planets located in distant stellar populations throughout the Milky Way (e.g., Penny et al. 2016; Ryu et al. 2018).

To date, six homogeneously selected statistical samples have been constructed for microlensing searches for bound planets (Gould et al. 2010; Cassan et al. 2012; Suzuki et al. 2016; Shvartzvald et al. 2016; Poleski et al. 2021; Zang et al. 2025). Among them, Zang et al. (2025) presents the largest sample, comprising 63 planets discovered by the Korea Microlensing Telescope Network (KMTNet; Kim et al. 2016) and its AnomalyFinder system (Zang et al. 2021a, 2022). Their analysis reveals two distinct populations of microlensing planets, a population of gas giants and a population of super-Earths/mini-Neptunes, and identifies a possible deficit in planet-to-host mass ratio (q) at $-3.6 < \log q < -3.0$. This potential “mass-ratio desert” may reflect the result of runaway gas accretion during planet formation (Ida & Lin 2004; Mordasini et al. 2009). The feature was later strengthened by investigating all KMTNet AnomalyFinder planets from 2016 to 2019 (Gui et al. 2024), although it was not apparent in the Microlensing Observations in Astrophysics (MOA, Sako et al. 2008) statistical sample, which contains 22 planets (Suzuki et al. 2016).

To further test the results of Zang et al. (2025), a larger sample is required. KMTNet monitors approximately 97 deg^2 of the Galactic bulge, including $\sim 13 \text{ deg}^2$ of prime fields with cadences of $\Gamma \geq 2 \text{ hr}^{-1}$ and $\sim 84 \text{ deg}^2$ of subprime fields with cadences of $\Gamma \leq 1 \text{ hr}^{-1}$. The field layout

and cadence distribution are shown in Figure 12 of Kim et al. (2018a). KMTNet identifies microlensing events through two channels. During the observing season, the KMTNet AlertFinder system (Kim et al. 2018b) scans the data every weekday to detect ongoing events in real time. In addition, after each season, the EventFinder system Kim et al. (2018a) analyzes the full yearly dataset and recovers hundreds of events missed by the real-time alerts. All discovered events are processed by the automatic pySIS pipeline (Albrow et al. 2009), yielding light curves based on the difference imaging analysis (DIA) technique (Tomaney & Crotts 1996; Alard & Lupton 1998).

Shin et al. (2026) have presented the complete KMTNet sample from all 2021 prime-field events, while Shin et al. (in prep.) and Ryu et al. (in prep.) will report results from the 2021 subprime- and 2022 prime-field datasets, respectively. For the 2023 season, we re-reduced all events with the optimized pySIS pipeline (Yang et al. 2024, 2025) and subsequently ran the AnomalyFinder on these reprocessed data. Besides published planets from by-eye searches (e.g., Han et al. 2024a,b, 2025), Ryu et al. (2026) have presented the full sample of low mass-ratio planets with $\log q < -3.7$ from the 2023 AlertFinder events. In this paper we present detailed analysis of six events, which reveals two secure planets, one brown dwarf, and three ambiguous candidates drawn from the 2023 prime-field AlertFinder sample. In addition, Li et al. (in prep.) will introduce an additional six events from the 2023 subprime-field AlertFinder sample. The planetary sample derived from the 2023 EventFinder search will be published in forthcoming papers.

2. OBSERVATIONS

Of the six events, four events, KMT-2023-BLG-1592, KMT-2023-BLG-0332/OGLE-2023-BLG-0317, KMT-2023-BLG-0332, and KMT-2023-BLG-0792/OGLE-2023-BLG-0604/MOA-2023-BLG-244, were first flagged by the KMTNet AlertFinder system. The remaining two events, OGLE-2023-BLG-0766/KMT-2023-BLG-1287 and OGLE-2023-BLG-1043/KMT-2023-BLG-1951/MOA-2023-BLG-395, were initially discovered by the Early Warning System (Udalski et al. 1994; Udalski 2003) of the Optical Gravi-

Table 1. Event Names, Alert, Locations, and Cadences for the five events analyzed in this paper

Event Name	First Alert Date	RA _{J2000}	Decl. _{J2000}	ℓ	b	Cadence	Method
KMT-2023-BLG-1592	10 Jul 2023	17:54:42.88	-29:00:30.31	+0.9583	-1.7446	2 hr ⁻¹	Recovery
OGLE-2023-BLG-0766	17 Jun 2023	17:59:19.11	-28:19:28.88	+2.0565	-2.2763	3 night ⁻¹	Discovery
KMT-2023-BLG-1287						4 hr ⁻¹	
KMT-2023-BLG-0332	10 Apr 2023	18:03:33.63	-27:13:20.60	+3.4796	-2.5481	4 hr ⁻¹	Discovery
OGLE-2023-BLG-0317						3 night ⁻¹	
KMT-2023-BLG-0486	20 Apr 2023	17:58:40.28	-26:54:34.60	+3.2130	-1.4474	2 hr ⁻¹	Discovery
KMT-2023-BLG-0792	12 May 2023	17:56:44.25	-30:36:55.12	-0.2114	-2.9315	4 hr ⁻¹	Discovery
OGLE-2023-BLG-0604						1 night ⁻¹	
MOA-2023-BLG-244						4 hr ⁻¹	
OGLE-2023-BLG-1043	04 Aug 2023	17:53:38.45	-28:53:51.61	+0.9350	-1.4860	1 hr ⁻¹	Discovery
KMT-2023-BLG-1951						4 hr ⁻¹	
MOA-2023-BLG-395						4 hr ⁻¹	

NOTE—“Discovery” indicates that the planet was discovered using AnomalyFinder, and “Recovery” means that the planet was first discovered from by-eye searches and then recovered by AnomalyFinder.

tational Lensing Experiment (OGLE; Udalski et al. 2015). Subsequently, the MOA survey also reported two events.

As described earlier, the KMTNet survey obtained data using its three telescopes located at KMTC, KMTS, and KMTA. The OGLE collaboration carried out observations from its 1.3 m telescope in Chile, which is equipped with a wide-field camera covering 1.4 deg² (Udalski et al. 2015). The MOA survey conducted observations with a 1.8 m telescope in New Zealand, featuring a camera with a field of view of 2.2 deg².

The majority of the KMTNet and OGLE data were acquired in the I band, whereas MOA observations were mainly carried out using the MOA-Red filter, a broad pass-band approximately equivalent to the combined Cousins R and I bands. In addition, each survey obtained a smaller number of images in the V band, which were used to determine the color of the source stars.

Table 1 provides an overview of the six microlensing events analyzed in this work, listing their event names, initial alert dates, equatorial and Galactic coordinates, the observing cadences of the participating surveys, as well as the anomaly identification method. Throughout this paper, each event is referred to by the designation under which it was first reported.

For the light-curve modeling, we adopted the photometric data products produced by the difference image analysis (DIA) pipelines of each survey: Albrow et al. (2009); Yang et al. (2024, 2025) for KMTNet, Wozniak (2000) for OGLE, and Bond et al. (2001) for MOA. The photometric error bars

were subsequently rescaled following the method described in Yee et al. (2012), such that each data set yields a reduced χ^2 of unity.

3. LIGHT-CURVE ANALYSIS

3.1. Preamble

In this section, we present the methodology used to model the observed microlensing light curves. While our overall strategy follows the general framework adopted in previous analyses of anomalous microlensing events (e.g., Zang et al. 2023), the implementation details and emphasis differ in several aspects. To maintain clarity and avoid unnecessary repetition, we provide here a concise but self-contained description of the modeling procedure, and refer interested readers to Zang et al. (2023) for a more comprehensive background discussion.

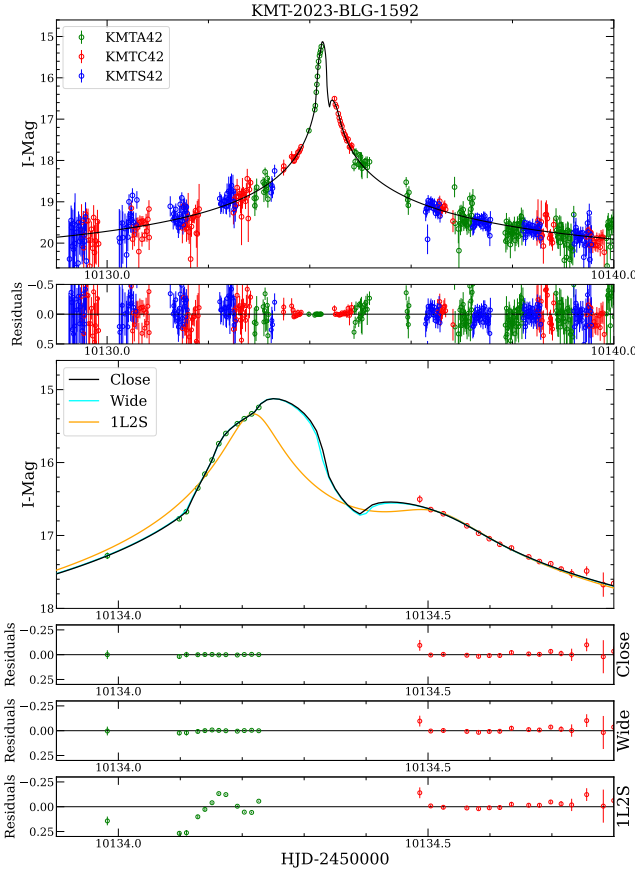
All events are firstly analyzed under the assumption of a static binary-lens single-source (2L1S) configuration. The model is specified by seven parameters. Three of these correspond to the standard point-source point-lens (PSPL, Paczyński 1986) description: the epoch of closest lens-source approach t_0 , the minimum impact parameter u_0 expressed in units of the angular Einstein radius θ_E , and the Einstein timescale t_E . The latter is related to the physical properties of the lens system through

$$t_E = \frac{\theta_E}{\mu_{\text{rel}}}, \quad \theta_E = \sqrt{\kappa M_L \pi_{\text{rel}}}, \quad (1)$$

Table 2. Lensing Parameters for KMT-2023-BLG-1592

Parameter	Wide	Close	1L2S
χ^2/dof	6756.0/6756	6752.2/6756	7607.6/6756
t_0 (HJD')	10134.259 ± 0.001	10134.260 ± 0.001	10134.217 ± 0.001
u_0 (10^{-4})	5.38 ± 1.37	5.17 ± 1.19	5.48 ± 0.84
t_E (days)	80.4 ± 17.3	91.7 ± 21.0	70.6 ± 11.6
ρ (10^{-4})	7.00 ± 1.54	6.15 ± 1.41	—
α (deg)	122.54 ± 0.47	122.19 ± 0.49	—
s	1.399 ± 0.007	0.700 ± 0.005	—
$\log q$	-3.010 ± 0.096	-3.017 ± 0.098	—
$t_{0,2}$ (HJD')	—	—	10134.508 ± 0.004
$u_{0,2}$ (10^{-4})	—	—	11.39 ± 1.93
$q_{f,I}$	—	—	0.3739 ± 0.0215
$I_{S,\text{KMTC}}$	23.389 ± 0.268	23.406 ± 0.242	23.284 ± 0.188

NOTE—HJD' = HJD - 2450000.

**Figure 1.** Light curves of KMT-2023-BLG-1592 with the 2L1S “Close”, “Wide” and the 1L2S models shown as solid black, cyan and yellow curves, respectively. The lower panel provides a zoom-in view of the anomaly. Data from different observatories are plotted in different colors. The corresponding lensing model parameters are listed in Table 2.

where $\kappa = 4G/(c^2 \text{ au}) \simeq 8.144 \text{ mas } M_{\odot}^{-1}$, M_L denotes the total lens mass, and π_{rel} and μ_{rel} are the lens-source relative parallax and proper motion, respectively.

Three parameters characterize the binary nature of the lens. These include the projected separation s between the two lens components normalized to θ_E , the mass ratio q , and the angle α between the source trajectory and the binary axis. Finally, finite-source effects (Gould 1994; Witt & Mao 1994; Nemiroff & Wickramasinghe 1994) are incorporated through the normalized source radius $\rho = \theta_*/\theta_E$, where θ_* is the angular radius of the source star.

Model light curves are computed using the contour-integration algorithm implemented in the `VBinaryLensing` package (Bozza 2010; Bozza et al. 2018, 2025). For each observatory data set i , the observed flux $f_i(t)$ is modeled as a linear combination of the magnified source flux and an additional blended component,

$$f_i(t) = f_{S,i} A(t) + f_{B,i}, \quad (2)$$

where $f_{S,i}$ and $f_{B,i}$ represent the source and blend fluxes, respectively.

To identify viable solutions, we combine a coarse and a dense exploration of parameter space using a multidimensional grid in $(\log q, \log s, \rho)$, while allowing (t_0, u_0, t_E, α) to vary continuously. Local minima are then refined through a Markov Chain Monte Carlo (MCMC) analysis of the χ^2 surface using the affine-invariant ensemble sampler `emcee` (Goodman & Weare 2010; Foreman-Mackey et al. 2013). The final parameter optimization is performed via downhill minimization with `SciPy` (Virtanen et al. 2020). In the vicinity of each local minimum, all parameters are allowed to vary freely. Parameter estimates reported throughout this

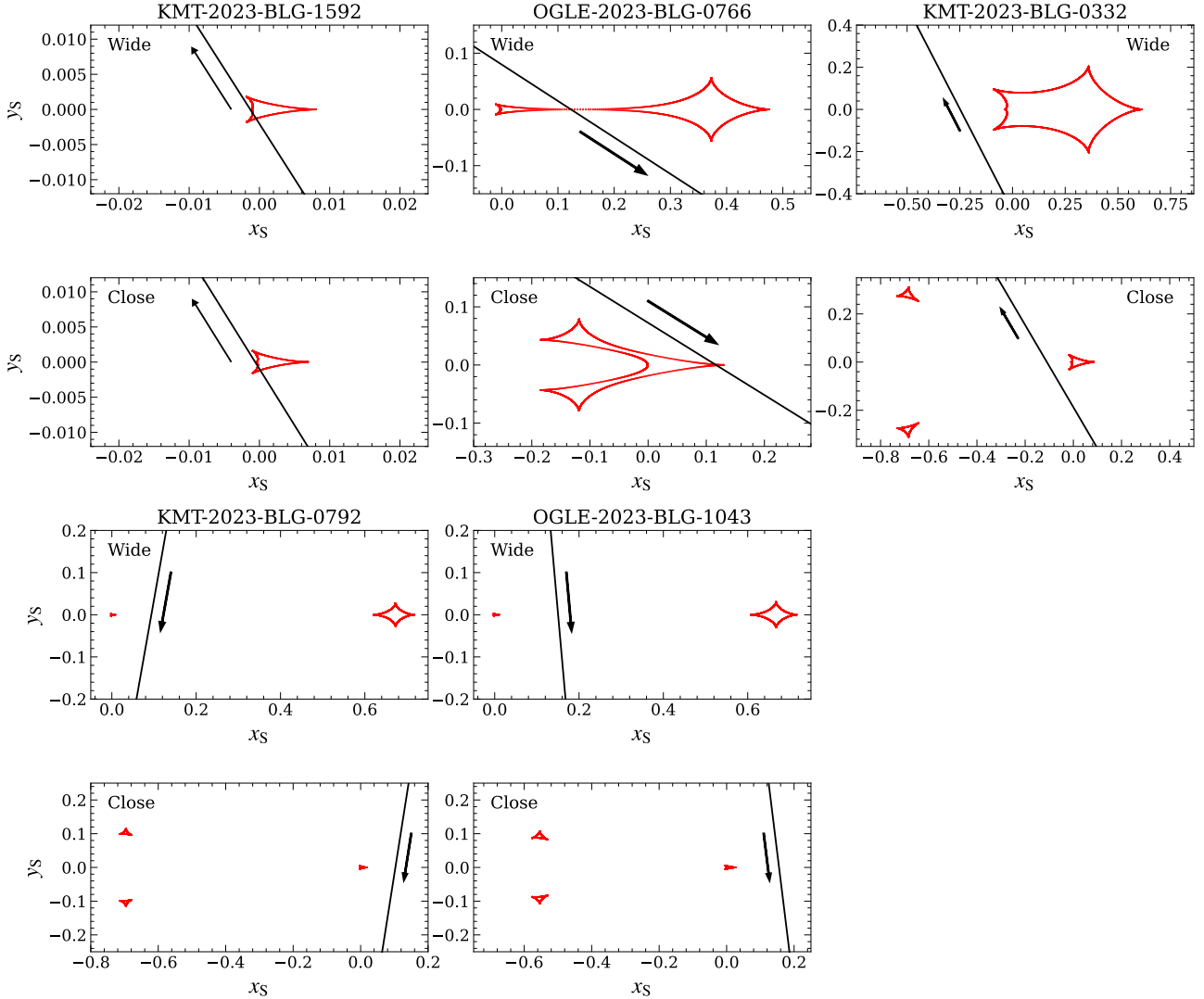


Figure 2. Geometries of the 2L1S solutions for KMT-2023-BLG-1592, OGLE-2023-BLG-0766, KMT-2023-BLG-0332, KMT-2023-BLG-0792, and OGLE-2023-BLG-1043, each of which exhibits a pair of “Close/Wide” degeneracies. For each event, the upper and lower panels display the corresponding “Wide” and “Close” solutions. In every panel, the red curves indicate the caustic structures, the black curve traces the source trajectory, and the arrow marks the direction of source motion.

work correspond to posterior median values, with uncertainties given by the central 68% credible intervals.

We further investigate whether annual microlensing parallax effects provide meaningful constraints for any of the events (Gould 1992, 2000, 2004). The microlensing parallax vector is defined as

$$\boldsymbol{\pi}_E = \frac{\pi_{\text{rel}} \boldsymbol{\mu}_{\text{rel}}}{\theta_E \mu_{\text{rel}}}, \quad (3)$$

and is parameterized by its north and east components ($\pi_{E,N}, \pi_{E,E}$). When parallax is included in the modeling, we also account for possible orbital motion of the lens system (Batista et al. 2011; Skowron et al. 2011) and explicitly explore both $u_0 > 0$ and $u_0 < 0$ solutions in order to cap-

ture the well-known ecliptic degeneracy (Jiang et al. 2004; Poindexter et al. 2005).

Because all events are characterized by smooth, bump-like deviations rather than dip-like anomalies, we additionally test a single-lens binary-source (1L2S) interpretation (Gaudi 1998). In this scenario, the observed magnification in a given photometric band λ is the flux-weighted sum of the magnifications of the two source stars (Hwang et al. 2013),

$$A_\lambda(t) = \frac{A_1(t)f_{S,1,\lambda} + A_2(t)f_{S,2,\lambda}}{f_{S,1,\lambda} + f_{S,2,\lambda}} = \frac{A_1(t) + q_{f,\lambda}A_2(t)}{1 + q_{f,\lambda}}, \quad (4)$$

where $q_{f,\lambda} = f_{S,2,\lambda}/f_{S,1,\lambda}$ is the source flux ratio and $A_j(t)$ ($j = 1, 2$) denotes the magnification of each source.

Following Zang et al. (2025), several studies have adopted $\Delta\chi^2 < 10$ as a criterion for identifying degenerate solutions (see also, e.g., Shin et al. 2023). In this work, we apply a more conservative threshold and exclude models with $\Delta\chi^2 > 20$. Because the $\Delta\chi^2$ values for all candidate solutions are explicitly reported, readers may readily impose alternative criteria depending on the requirements of specific statistical analyses or population studies.

Below, we first present three unambiguous 2L1S events and then introduce three additional events that can be described by both 2L1S and 1L2S models.

3.2. KMT-2023-BLG-1592

The anomaly of KMT-2023-BLG-1592, as shown in Figure 1, is a bump-type feature near the peak, captured by the KMTA42 data. The grid search finds only a pair of solutions, although there is a 0.25 day gap between the KMTA42 and KMTC42 data over the peak. Following standard convention, we denote these solutions as “Close” and “Wide” corresponding to projected separations of $s < 1$ and $s > 1$, respectively (Griest & Safizadeh 1998). The 2L1S parameters for each solution are presented in Table 2, and the $\Delta\chi^2$ between the two solutions is only 3.8. As shown in the lower panels of Figure 1, both solutions provide good fits to the data. The caustic topology is shown in Figure 2. The anomaly is produced by a source caustic crossing of the central caustic.

The source star is very faint, with $I_S = 23.4$, so the peak magnification reaches ~ 2100 , making this one of the highest-magnification microlensing events (Dong et al. 2006; Gould et al. 2009; Yee et al. 2009; Zang et al. 2021b), although the uncertainty of the source magnitude is large. Finite-source effects are detected in both solutions, although the data cover only about half of the anomaly.

Because the anomaly shows a secondary rise rather than a single bump, the 1L2S model is strongly rejected, with $\Delta\chi^2 = 855$. Due to the very faint source, this event provides no useful constraint on the parallax, with $1-\sigma$ uncertainties in the parallax vector 0.4 in all directions. With $\log q \sim -3.0$, this event reveals a new gas giant.

3.3. OGLE-2023-BLG-0766

As shown in Figure 3, the anomaly of OGLE-2023-BLG-0766 appears as a short-lived bump about six days after the main peak. It is primarily characterized by the KMTA data, with additional support from KMTC. The grid search yields two local minima. Their caustic geometries and source trajectories are shown in Figure 2, and the corresponding 2L1S lensing parameters are listed in Table 3. The anomaly is produced by a source crossing of a resonant caustic, and we therefore refer to the two solutions as the “Close” and “Wide” models. Both solutions provide similarly good fits to the data, with a χ^2 difference of only 0.4. Finite-source effects are measured in both cases.

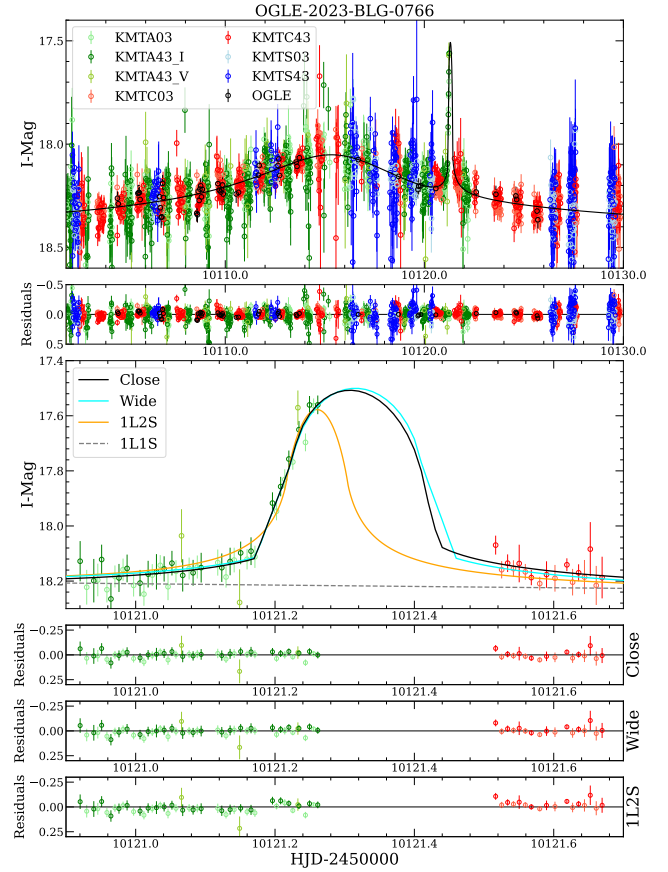


Figure 3. The observed data and models for OGLE-2023-BLG-0766. The symbols are similar to those in Figure 1.

The 1L2S model is disfavored by $\Delta\chi^2 = 25.5$, which is statistically significant. As shown in Figure 3, the 1L2S model mainly fails to reproduce the wings of the anomaly. In addition, the 1L2S model could be verified by searching for a color change during the anomaly, since a difference in the colors of the two sources would produce chromatic variations (Mao & Paczynski 1991; Gaudi 1998). A single KMTA43 V -band data point obtained near the peak of the anomaly constrains the color of the secondary source. As discussed in Section 4.3, the inferred color places the putative secondary source away from the main-sequence branch, further excluding the 1L2S interpretation.

Due to the faintness of the event, the microlensing parallax is poorly constrained, with $1-\sigma$ uncertainties in the parallax vector > 1 in all directions. We therefore adopt the static 2L1S model as the final interpretation of this event. With $\log q \sim -2.6$, the lens companion is consistent with a gas giant planet.

3.4. KMT-2023-BLG-0332

The anomaly of KMT-2023-BLG-0332, as shown in Figure 4, is an asymmetric feature near the peak, captured by both the KMTNet and OGLE data. The grid search yields

Table 3. Lensing Parameters for OGLE-2023-BLG-0766

Parameters	Wide	Close	1L2S
χ^2/dof	14084.7/14088	14084.3/14088	14109.8/14088
t_0 (HJD')	10115.56 ± 0.06	10115.57 ± 0.05	10115.08 ± 0.05
u_0	0.0731 ± 0.0011	0.0669 ± 0.0067	0.0519 ± 0.0080
t_E (days)	52.2 ± 6.1	55.0 ± 3.8	69.5 ± 10.2
$\rho(10^{-3})$	1.14 ± 0.17	1.00 ± 0.17	—
α (deg)	326.89 ± 0.76	327.50 ± 0.88	—
s	1.204 ± 0.026	0.942 ± 0.011	—
$\log q$	-2.564 ± 0.036	-2.589 ± 0.045	—
$t_{0,2}$ (HJD')	—	—	10121.26 ± 0.01
$u_{0,2}(10^{-4})$	—	—	1.00 ± 0.70
$\rho_2(10^{-3})$	—	—	0.66 ± 0.10
$q_{f,I}$	—	—	0.0131 ± 0.0012
$q_{f,V}$	—	—	0.0180 ± 0.0054
$I_{S,KMTC}$	22.058 ± 0.183	22.034 ± 0.112	22.658 ± 0.187

a pair of “Close/Wide” solutions. As shown in Figure 2, the anomaly is produced by a cusp approach to the central caustic (for “Close”) or to the resonant caustic (for “Wide”). According to the lensing parameters listed in Table 4, the “Wide” solution provides the best fit, with a brown dwarf mass ratio of $\log q = -1.404 \pm 0.054$. The “Close” solution has a planetary mass ratio of $\log q = -1.732 \pm 0.029$ and is disfavored by $\Delta\chi^2 = 30$, which is sufficient to reject it. No useful constraint on finite-source effects is obtained, with the $1\text{-}\sigma$ upper limit on ρ exceeding 0.01.

The 1L2S model, whose parameters are also listed in Table 4, is strongly excluded, with $\Delta\chi^2 = 219$. Because of the extended demagnified region following the cusp approach, the anomaly does not exhibit a typical bump-type morphology. Due to the faintness of the event, with a peak brightness of only $I \sim 19$ mag, no meaningful constraint on parallax can be derived from the data.

With $\log q = -1.404 \pm 0.054$, the companion is likely a brown dwarf. Therefore, this event is not included in the study of the planetary mass-ratio function, but it can be incorporated into future statistical analysis of brown dwarf companions.

3.5. KMT-2023-BLG-0486

Figure 5 shows the KMTNet light curve of KMT-2023-BLG-0486 obtained from its three observatory sites. The event largely follows a standard PSPL morphology, but exhibits an additional smooth, low-amplitude bump approximately 14 days prior to peak magnification. This anomaly persists for about five days with a peak amplitude of ~ 0.1 mag.

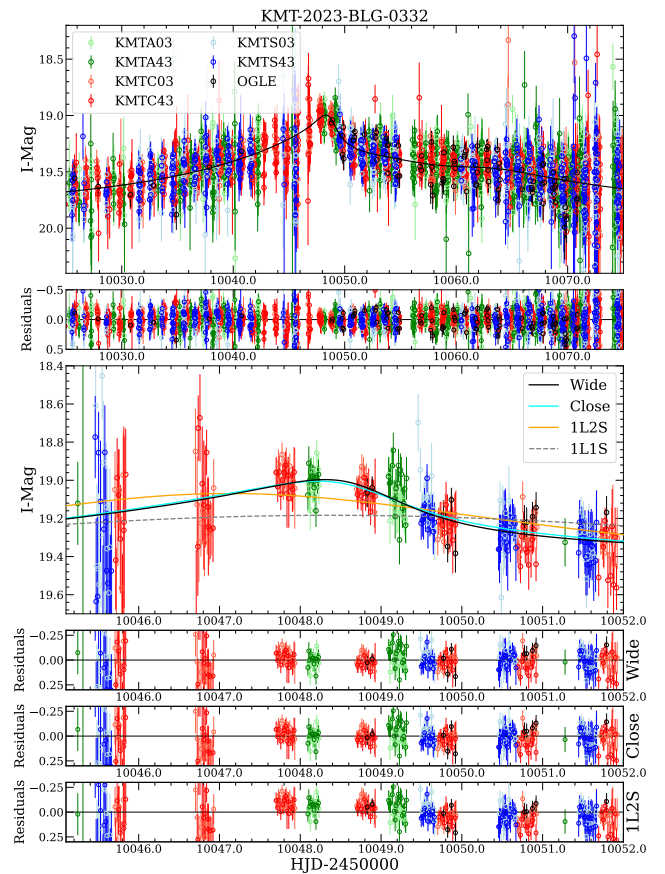
**Figure 4.** The observed data and models for KMT-2023-BLG-0332. The symbols are similar to those in Figure 1.

Table 4. Lensing parameters for KMT-2023-BLG-0332

Parameter	Wide	Close	1L2S
χ^2/dof	13106.5/13110	13136.5/13110	13325.4/13110
t_0 (HJD')	10050.50 ± 0.19	10049.68 ± 0.12	10047.02 ± 0.09
u_0	0.2061 ± 0.0309	0.0908 ± 0.0079	0.0279 ± 0.0066
t_E (days)	45.23 ± 4.96	81.16 ± 6.93	146.70 ± 32.48
α (deg)	117.48 ± 0.80	120.64 ± 0.63	—
s	1.197 ± 0.032	0.705 ± 0.004	—
$\log q$	-1.404 ± 0.054	-1.732 ± 0.029	—
$t_{0,2}$ (HJD')	—	—	10063.49 ± 0.41
$u_{0,2}$	—	—	0.0412 ± 0.0119
$q_{f,I}$	—	—	0.3375 ± 0.0509
$I_{S,\text{KMTC}}$	21.508 ± 0.186	22.429 ± 0.096	23.669 ± 0.346

Table 5. Lensing Parameters for KMT-2023-BLG-0486

Parameter	Wide	Close	Off-axis	1L2S
χ^2/dof	6296.4/6297	6296.1/6297	6327.2/6297	6290.6/6297
t_0 (HJD')	10078.33 ± 0.03	10078.26 ± 0.04	10078.96 ± 0.08	10078.60 ± 0.03
u_0	0.0240 ± 0.0063	0.0396 ± 0.0079	-0.0625 ± 0.0030	0.0412 ± 0.0046
t_E (days)	217.8 ± 61.9	128.9 ± 28.5	82.8 ± 3.9	118.3 ± 13.6
$\rho(10^{-2})$	—	—	2.73 ± 0.76	—
α (deg)	199.1 ± 0.3	198.9 ± 0.4	5.63 ± 0.82	—
s	1.224 ± 0.018	0.882 ± 0.016	0.912 ± 0.021	—
$\log q$	-3.238 ± 0.125	-2.930 ± 0.130	-2.558 ± 0.047	—
$t_{0,2}$ (HJD')	—	—	—	10064.63 ± 0.16
$u_{0,2}$	—	—	—	0.0116 ± 0.0040
$q_{f,I}$	—	—	—	0.0232 ± 0.0037
$I_{S,\text{KMTC}}$	22.118 ± 0.274	21.588 ± 0.212	21.143 ± 0.050	21.740 ± 0.179

Our grid search identifies three distinct local minima in parameter space, whose corresponding caustic geometries are illustrated in Figure 6. In two of these solutions, which are labeled as “Close” and “Wide”, the anomaly arises from a cusp approach associated with the central caustic. In the third solution, the bump is produced by an off-axis caustic crossing involving the central caustic, we therefore label this configuration as “Off-axis”. Similar off-axis solutions have been reported in previous KMTNet events, such as KMT-2019-BLG-1216 (Jung et al. 2023).

The posterior parameters derived from the MCMC analysis are summarized in Table 5. Among the three solutions, the “Close” solution yields the best fit to the data, while the “Wide” solution is only marginally worse, with $\Delta\chi^2 = 0.3$. In contrast, the “Off-axis” solution is strongly

disfavored, with $\Delta\chi^2 = 31.3$. This discrepancy is evident in the zoomed-in view of the anomaly shown in Figure 5, in which the “Off-axis” model is worse to reproduce the observed bump, particularly near $\text{HJD}' \simeq 10065$ (where $\text{HJD}' \equiv \text{HJD} - 2450000$). Moreover, the “Off-axis” solution requires significant finite-source effects, with a normalized source radius of $\rho = (2.85 \pm 0.36) \times 10^{-2}$. When combined with the extinction $A_I \sim 2.7$ based on the Nataf et al. (2013) extinction map and the source-property analysis routine described in Section 4, this implies an exceptionally low lens-source relative proper motion of $\mu_{\text{rel}} \sim 0.05 \text{ mas yr}^{-1}$. Based on Equation (9) of Jung et al. (2022), which is derived from the observed μ_{rel} distribution of planetary microlensing events (Gould 2022), the probability of such a low proper motion is only $\sim 7 \times 10^{-5}$. We therefore regard the “Off-

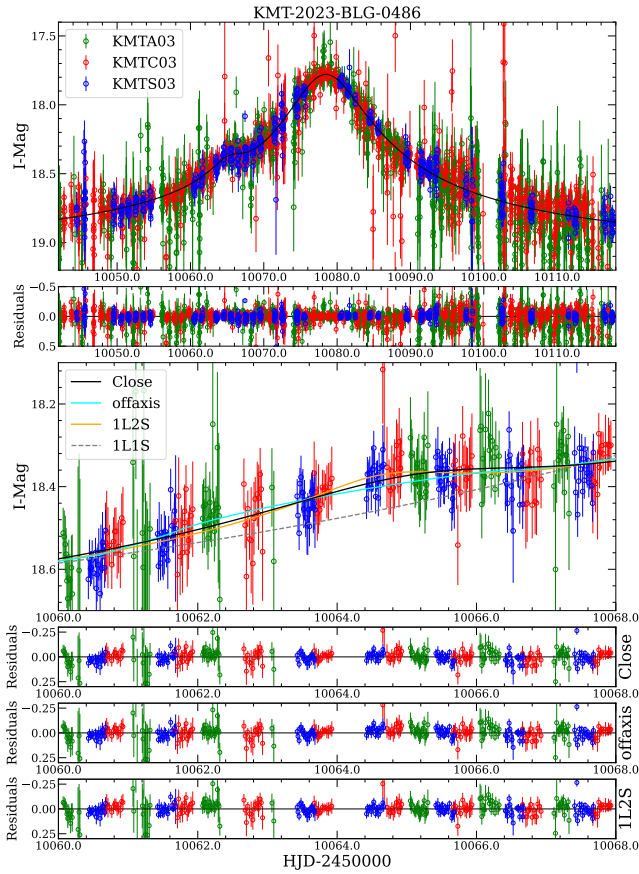


Figure 5. Light curves and models for KMT-2023-BLG-0486. The symbols are similar to those in Figure 1.

axis” solution as physically implausible and exclude it from further consideration.

The 1L2S model is favored over the 2L1S model by $\Delta\chi^2 = 5.5$. Finite-source effects are not detected for either source, and therefore the 1L2S interpretation cannot be tested via the implied lens-source relative proper motion. In addition, the event lies in a region of relatively high extinction, with $A_I \sim 2.7$, and the anomaly is only weakly magnified, so the V -band data taken during the anomaly provide no useful constraint on the source color. Hence, the 1L2S interpretation cannot be tested using color information.

In conclusion, the lens-source system could be described by either a 2L1S or a 1L2S model. Because this is only a candidate planetary event, we do not pursue further analysis.

3.6. KMT-2023-BLG-0792

Figure 7 shows the observed data for KMT-2023-BLG-0792, including six KMTNet data sets as well as data from the OGLE and MOA surveys. The anomaly appears as an asymmetric peak near the PSPL maximum and is covered by all data sets. The 2L1S grid search yields only a pair of solutions that exhibit the “Close/Wide” typology. As shown in Figure 2, the anomaly is produced by a cusp approach to

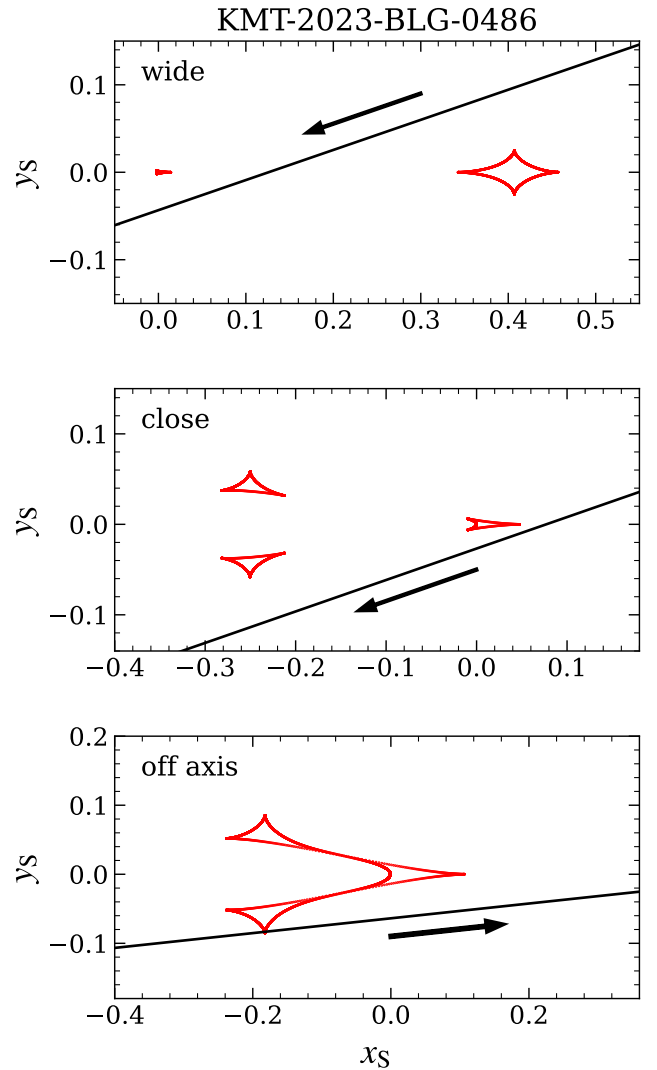


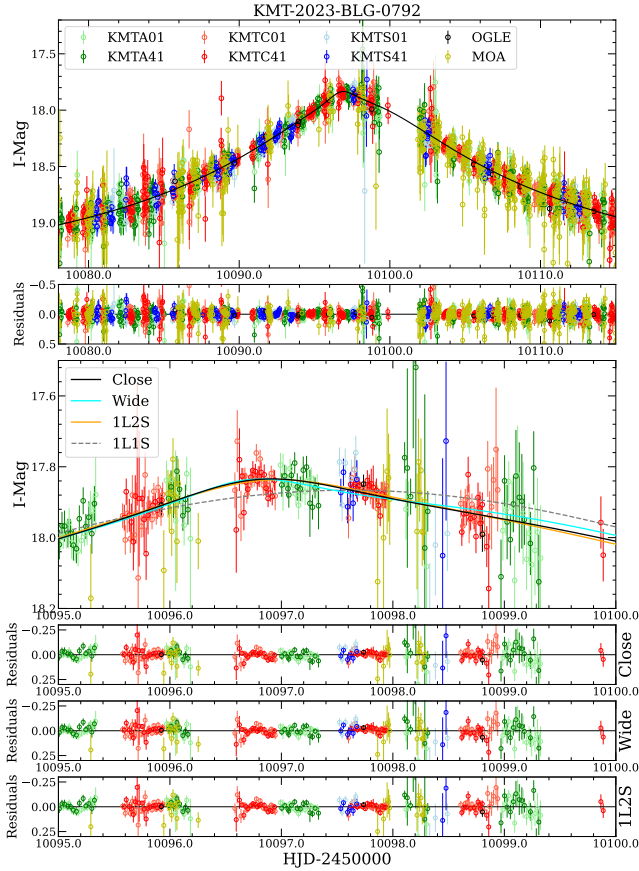
Figure 6. Geometries of the 2L1S models for KMT-2023-BLG-0486. The symbols are similar to those in Figure 2.

the central caustic. Table 5 presents the lensing parameters. The “Close” solution provides the best fit, while the “Wide” solution is disfavored by $\Delta\chi^2 = 15.1$. According to our criterion, the “Wide” solution cannot be definitively ruled out. Finite-source effects are not well constrained for either solution, with $1-\sigma$ upper limits on ρ exceeding 0.02. We therefore adopt the point-source model parameters.

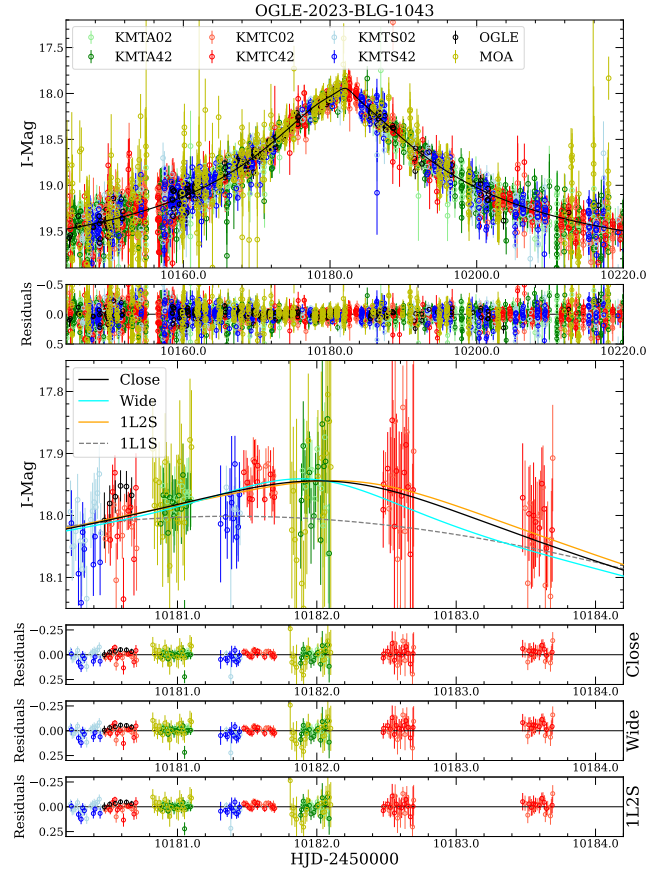
The 1L2S model provides a slightly better fit than the 2L1S “Close” model, with $\Delta\chi^2 = 4.6$. The finite-source effect of the secondary source is consistent with a point-source model within 1σ , so the 1L2S model cannot be tested using the “kinematic argument”. In addition, due to the faintness of the event, the V -band data obtained over the anomaly have signal-to-noise ratios (SNR) below 10, which are insufficient to test the 1L2S interpretation through the measured color of the secondary source.

Table 6. Lensing Parameters for KMT-2023-BLG-0792

Parameter	Wide	Close	1L2S
χ^2/dof	11445.8/11452	11430.7/11452	11426.1/11452
t_0 (HJD')	10097.561 ± 0.021	10097.569 ± 0.018	10097.643 ± 0.025
u_0	0.0924 ± 0.003	0.0998 ± 0.003	0.116 ± 0.006
t_E (days)	54.05 ± 1.53	51.42 ± 1.46	49.32 ± 1.54
α (deg)	260.14 ± 0.85	261.03 ± 0.71	—
s	1.392 ± 0.008	0.710 ± 0.008	—
$\log q$	-2.99 ± 0.04	-2.60 ± 0.05	—
$t_{0,2}$ (HJD')	—	—	10096.86 ± 0.05
$u_{0,2}$	—	—	0.0229 ± 0.0031
$q_{f,I}$	—	—	0.0428 ± 0.0093
$I_{S,\text{KMTc}}$	20.610 ± 0.039	20.520 ± 0.068	20.470 ± 0.047

**Figure 7.** Light curves and models for KMT-2023-BLG-0792. The symbols are similar to those in Figure 1.

For this event, the parallax contours take the form of elongated ellipses. The constraint along the minor axis of the error ellipse is meaningful, with $\sigma(\pi_{E,\parallel}) = 0.15$, where the parallel direction is approximately aligned with the Earth's

**Figure 8.** Light curves and models for OGLE-2023-BLG-1043. The symbols are similar to those in Figure 1.

acceleration. However, because the event can be modeled as either 2L1S or 1L2S, we do not pursue further analysis.

3.7. OGLE-2023-BLG-1043

Table 7. Lensing Parameters for OGLE-2023-BLG-1043

Parameter	Wide	Close	1L2S
χ^2/dof	15672.0/15677	15657.0/15677	15649.0/15677
t_0 (HJD')	10181.37 ± 0.02	10181.36 ± 0.02	10181.27 ± 0.04
u_0	0.150 ± 0.04	0.153 ± 0.004	0.172 ± 0.007
t_E (days)	44.42 ± 0.84	43.79 ± 0.84	42.38 ± 0.98
α (deg)	275.00 ± 1.05	276.71 ± 1.02	—
s	1.39 ± 0.01	0.76 ± 0.02	—
$\log q$	-2.896 ± 0.053	-2.583 ± 0.05	—
$t_{0,2}$ (HJD')	—	—	10182.24 ± 0.10
$u_{0,2}$	—	—	0.032 ± 0.007
$q_{f,I}$	—	—	0.032 ± 0.010
$I_{S,KMTC}$	20.120 ± 0.033	20.093 ± 0.031	20.053 ± 0.040

The anomaly is also an asymmetric peak, as shown in Figure 8. Compared to the 1L1S model (the grey dashed line), the anomaly appears as a bump-type feature occurring slightly after the 1L1S peak, and its overall morphology is similar to that of KMT-2023-BLG-0792. Therefore, both 2L1S and 1L2S models are considered. For the 2L1S interpretation, a pair of ‘‘Close/Wide’’ solutions is found. The ‘‘Close’’ solution provides the best fit, while the ‘‘Wide’’ solution is disfavored by $\Delta\chi^2 = 15.0$, as listed in Table 7. The anomaly is also produced by a cusp approach to the central caustic, as shown in Figure 2.

The 1L2S model is favored by $\Delta\chi^2 = 8.0$ relative to the 2L1S ‘‘Close’’ model. For the same reasons as in KMT-2023-BLG-0792, the 1L2S model cannot be rejected based on the derived lens-source relative proper motion or the color of the putative secondary source. Therefore, for this event, both 2L1S and 1L2S models can explain the observations, and we do not pursue further analysis.

4. SOURCE AND LENS PROPERTIES

4.1. Preamble

We determine the lens physical properties of three unambiguous 2L1S events, KMT-2023-BLG-1592, OGLE-2023-BLG-0766, and KMT-2023-BLG-0332, in this section. Following the procedure outlined in Section 3.1, we first describe the general methodology.

The lens mass M_L and distance D_L are expressed in terms of the angular Einstein radius and the microlensing parallax (Gould 1992, 2000) as

$$M_L = \frac{\theta_E}{\kappa\pi_E}; \quad D_L = \frac{\text{au}}{\pi_E\theta_E + \pi_S}, \quad (5)$$

where π_S denotes the source parallax. The angular Einstein radius can be obtained from $\theta_E = \theta_*/\rho$. To evaluate θ_* , we place the source on the $V - I$ versus I color-

magnitude diagram (CMD; Yoo et al. 2004) constructed from OGLE-III stars within a $2'$ radius centered on the event (Szymański et al. 2011). The centroid of the red clump (RC), $(V - I, I)_{RC}$, is derived using the method of Nataf et al. (2013), and its intrinsic color and magnitude, $(V - I, I)_{RC,0}$, are adopted from Bensby et al. (2013) and Table 1 of Nataf et al. (2013). Then, the total extinction in the I band and the reddening toward each event are derived as

$$[E(V - I), A_I] = [(V - I, I)_{RC}] - [(V - I, I)_{RC,0}]. \quad (6)$$

For each event, the apparent source magnitude is obtained from the light-curve modeling and calibrated to the OGLE-III photometric system using common field stars between KMTNet and OGLE-III. For KMT-2023-BLG-1592 and OGLE-2023-BLG-0766, the source color $(V - I)_S$ is determined from a regression of the KMTNet V -band and I -band fluxes as a function of magnification and then calibrated to the OGLE-III color scale. The intrinsic source magnitude and color are thus derived as

$$[(V - I), I]_{S,0} = [(V - I), I]_S - [E(V - I), A_I]. \quad (7)$$

For KMT-2023-BLG-0332, because of the low SNR in the V band, we determine the source color by aligning the *Hubble Space Telescope* (*HST*) CMD from Holtzman et al. (1998) to the OGLE-III CMD using the measured I_{cl} of the red clump. The source color is then estimated from *HST* field stars within $5\text{-}\sigma$ of the source brightness. Applying the color/surface-brightness relation of Adams et al. (2018), we obtain θ_* , which leads to measurements of θ_E and μ_{rel} .

Figure 9 displays the CMDs of the three events, and Table 8 summarizes the corresponding CMD parameters, source properties, θ_E , and μ_{rel} for all solutions.

Among the three events, none of events have useful constraints on the microlensing parallax. We therefore infer the

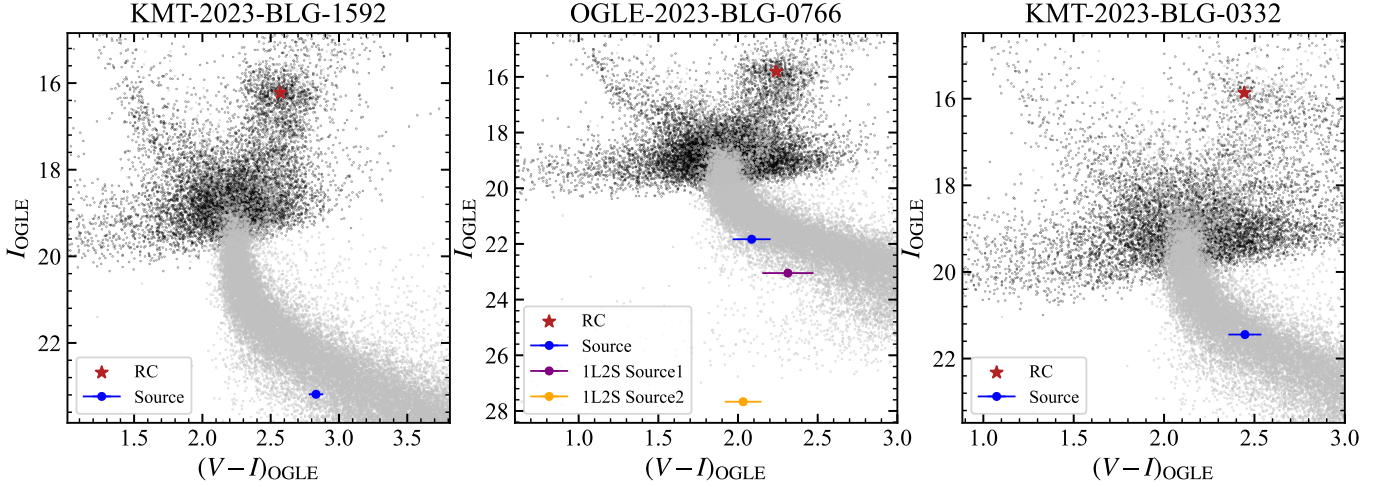


Figure 9. Color-magnitude diagrams of the three unambiguous 2L1S events, constructed using OGLE-III stars within a $2'$ radius centered on each event (Szymański et al. 2011). In each panel, the red asterisk marks the centroid of the red clump, and the blue dot indicates the 2L1S source star. For OGLE-2023-BLG-0766, the two 1L2S source stars are also shown. The grey dots represent the *HST* CMD from Holtzman et al. (1998). The centroid of the red-giant clump in the *HST* CMD, $(V - I, I)_{\text{cl},\text{HST}} = (1.62, 15.15)$ (Bennett et al. 2008), is aligned with that of the OGLE-III CMD.

Table 8. CMD parameters, source properties and derived θ_E and μ_{rel}

Parameter	KMT-2023-BLG-1592		OGLE-2023-BLG-0766		KMT-2023-BLG-0332
	Wide	Close	Wide	Close	
I_{RC}	16.22 ± 0.02	←	15.81 ± 0.03	←	15.86 ± 0.06
$(V - I)_{\text{RC}}$	2.57 ± 0.01	←	2.24 ± 0.01	←	2.44 ± 0.01
$I_{\text{RC},0}$	14.40 ± 0.04	←	14.37 ± 0.04	←	14.34 ± 0.04
$(V - I)_{\text{RC},0}$	1.06 ± 0.03	←	←	←	←
I_{S}	23.16 ± 0.27	23.18 ± 0.25	21.92 ± 0.20	21.83 ± 0.13	21.44 ± 0.20
$(V - I)_{\text{S}}$	2.83 ± 0.05	←	2.08 ± 0.12	←	2.45 ± 0.11
$I_{\text{S},0}$	21.33 ± 0.27	21.36 ± 0.25	20.48 ± 0.20	20.40 ± 0.14	19.92 ± 0.21
$(V - I)_{\text{S},0}$	1.32 ± 0.06	←	0.90 ± 0.12	←	1.07 ± 0.12
θ_* (μas)	0.298 ± 0.043	0.294 ± 0.040	0.307 ± 0.045	0.319 ± 0.041	0.457 ± 0.068
θ_E (mas)	0.425 ± 0.112	0.478 ± 0.127	0.318 ± 0.069	0.319 ± 0.042	—
μ_{rel} (mas yr^{-1})	1.930 ± 0.654	1.901 ± 0.667	1.889 ± 0.453	2.113 ± 0.479	—

physical parameters of the systems through a Bayesian analysis that adopts a Galactic model as the prior. The model assumptions and computational framework follow Yang et al. (2021), including the assumption that the planet occurrence rate does not depend on host-star properties such as mass. Additional details are given in that work.

The posterior distributions from the Bayesian analysis are summarized in Table 9 and illustrated in Figure 10. These include the host mass M_{host} , planet mass M_{planet} , lens distance D_L , projected lens separation r_{\perp} , and the heliocentric lens-source relative proper motion $\mu_{\text{hel,rel}}$.

4.2. KMT-2023-BLG-1592

The intrinsic source color and magnitude are $[(V - I), I]_{\text{S},0} = [1.10 \pm 0.04, 20.68 \pm 0.17]$. Based on its position relative to the *HST* field stars in Figure 9, the source is likely a metal-poor K dwarf located in the bulge. The lens-source relative proper motion, $\sim 1.9 \text{ mas yr}^{-1}$, is normal for a planetary event (Gould 2022).

The Bayesian analysis indicates that the host is likely an M- or K-dwarf. The planetary mass is $\sim 0.6 M_{\text{Jupiter}}$, and the projected planet-host separation is $\sim 4 \text{ au}$ for the “Wide” solution and $\sim 2 \text{ au}$ for the “Close” solution. Adopting a water snow-line scaling of $a_{\text{SL}} = 2.7(M/M_{\odot}) \text{ au}$ (Kennedy & Kenyon 2008), the planet lies well beyond the snow line in

Table 9. Lensing Physical Parameters from Bayesian Analyses

Event	Model	$M_{\text{host}} (M_{\odot})$	$M_{\text{planet}} (M_{\text{Jupiter}})$	D_L (kpc)	r_{\perp} (au)	$\mu_{\text{rel, hel}}$ (mas yr $^{-1}$)
KMT-2023-BLG-1592	Close	$0.59^{+0.33}_{-0.29}$	$0.57^{+0.37}_{-0.29}$	$7.0^{+1.1}_{-2.2}$	$2.1^{+0.6}_{-0.6}$	$2.54^{+1.59}_{-0.88}$
	Wide	$0.55^{+0.33}_{-0.27}$	$0.58^{+0.39}_{-0.29}$	$7.2^{+1.1}_{-1.9}$	$3.9^{+1.1}_{-1.1}$	$2.48^{+1.31}_{-0.80}$
OGLE-2023-BLG-0766	Close	$0.45^{+0.32}_{-0.22}$	$1.20^{+0.86}_{-0.60}$	$7.3^{+0.9}_{-1.1}$	$2.2^{+0.5}_{-0.5}$	$2.19^{+0.51}_{-0.46}$
	Wide	$0.39^{+0.30}_{-0.20}$	$1.10^{+0.87}_{-0.57}$	$7.4^{+0.9}_{-0.9}$	$2.5^{+0.6}_{-0.6}$	$2.11^{+0.55}_{-0.47}$
KMT-2023-BLG-0332	—	$0.54^{+0.38}_{-0.30}$	$22.0^{+15.7}_{-12.2}$	$6.5^{+1.2}_{-2.8}$	$3.2^{+1.3}_{-1.2}$	$3.93^{+2.82}_{-1.60}$

the “Wide” solution and may reside near the snow line in the “Close” solution.

4.3. OGLE-2023-BLG-0766

For this event, the CMD also helps exclude the 1L2S model. As shown in Figure 9, we plot the two 1L2S source stars. The hypothetical secondary source would be extremely faint, $I \sim 27.6$, and significantly bluer than the main-sequence branch. Such a position in the CMD is physically implausible, rendering the 1L2S interpretation unlikely.

The Bayesian analysis indicates that the host star is most likely an M-dwarf. The planet has approximately Jupiter mass, and the projected planet-host separation is ~ 2.3 au. Therefore, this gas-giant planet is also beyond the snow line.

4.4. KMT-2023-BLG-0332

For this event, ρ is not usefully constrained, and therefore no meaningful constraints can be placed on θ_E or μ_{rel} . Nevertheless, we derive the source properties from the CMD, as this information may assist in planning high-resolution follow-up observations. The source is 5.6 mag fainter than the red clump, suggesting that it is likely a K-dwarf and therefore unlikely to be a bright blend relative to the lens in future high-resolution imaging.

The Bayesian analysis indicates that the host is also likely an M- or K-dwarf. The companion mass is $22.0^{+15.7}_{-12.2} M_{\text{Jupiter}}$, implying that it is most likely a low-mass brown dwarf. The lens-source relative proper motion is $3.93^{+2.82}_{-1.60}$ mas yr $^{-1}$.

5. DISCUSSION

We have presented the observations and analysis of six anomalous microlensing events located in the KMTNet prime field. Among them, three are securely classified as 2L1S events, including two planetary systems and one brown dwarf system, while the remaining three exhibit the 2L1S/1L2S degeneracy. For the three confirmed 2L1S events, the anomaly in KMT-2023-BLG-1592 was initially identified through by-eye searches, whereas the anomalies in all three 2L1S/1L2S cases were detected by the AnomalyFinder system.

Since the 1L2S degeneracy in planetary microlensing events was first identified by Gaudi (1998), it has remained

the most common ambiguity in planetary interpretations (e.g., Hwang et al. 2013; Shin et al. 2019). In constructing the largest microlensing planetary statistical sample (Zang et al. 2025), 11 of 63 candidate planets were excluded due to the 2L1S/1L2S degeneracy¹, corresponding to a degeneracy fraction of 17.5%. Of these 11 events, eight were first identified by AnomalyFinder and three via by-eye searches, yielding an AnomalyFinder discovery fraction of 72.7%, substantially higher than the $\sim 33\%$ rate for unambiguous planets (Gui et al. 2024). This trend is expected because AnomalyFinder is more sensitive to subtle anomalies, for which the lower SNRs makes them harder to distinguish from 1L2S solutions using light curves’ χ^2 , color, or kinematic constraints.

With the upcoming Nancy Grace Roman Space Telescope (Penny et al. 2019) and the Earth 2.0 Microlensing Telescope (ET) (Gould et al. 2021; Ge et al. 2022), the number of detected planetary microlensing events per year is expected to increase dramatically. The systematic discovery of planets by AnomalyFinder underscores its importance for future survey data analysis. At the same time, the high 2L1S/1L2S degeneracy rate within the AnomalyFinder sample calls for particular caution when interpreting planetary signals with bump-type features.

Our analysis also identifies a brown dwarf event with $\log q = -1.4$. At present, only one homogeneous microlensing sample probes the brown dwarf mass-ratio regime, $-1.5 < \log q < -1.0$, based on Wise, OGLE, and MOA data (Shvartzvald et al. 2016), although the number of events in that sample remains small. Current KMTNet statistical studies primarily focus on planetary companions with $\log q < -1.5$. Ongoing analyses of brown-dwarf systems discovered through by-eye searches are reported in (Han et al. 2020, 2022, 2023a,b, 2024c). A future systematic study of brown dwarf events identified by AnomalyFinder could extend the KMTNet mass-ratio function toward $\log q \sim -1$.

¹ Zang et al. (2025) reported nine such cases, and two additional events, OGLE-2018-BLG-1554 (Gould et al. 2022b) and OGLE-2019-BLG-0344 (Jung et al. 2023), excluded for degenerate binary-star solutions, also exhibit 1L2S degeneracy.

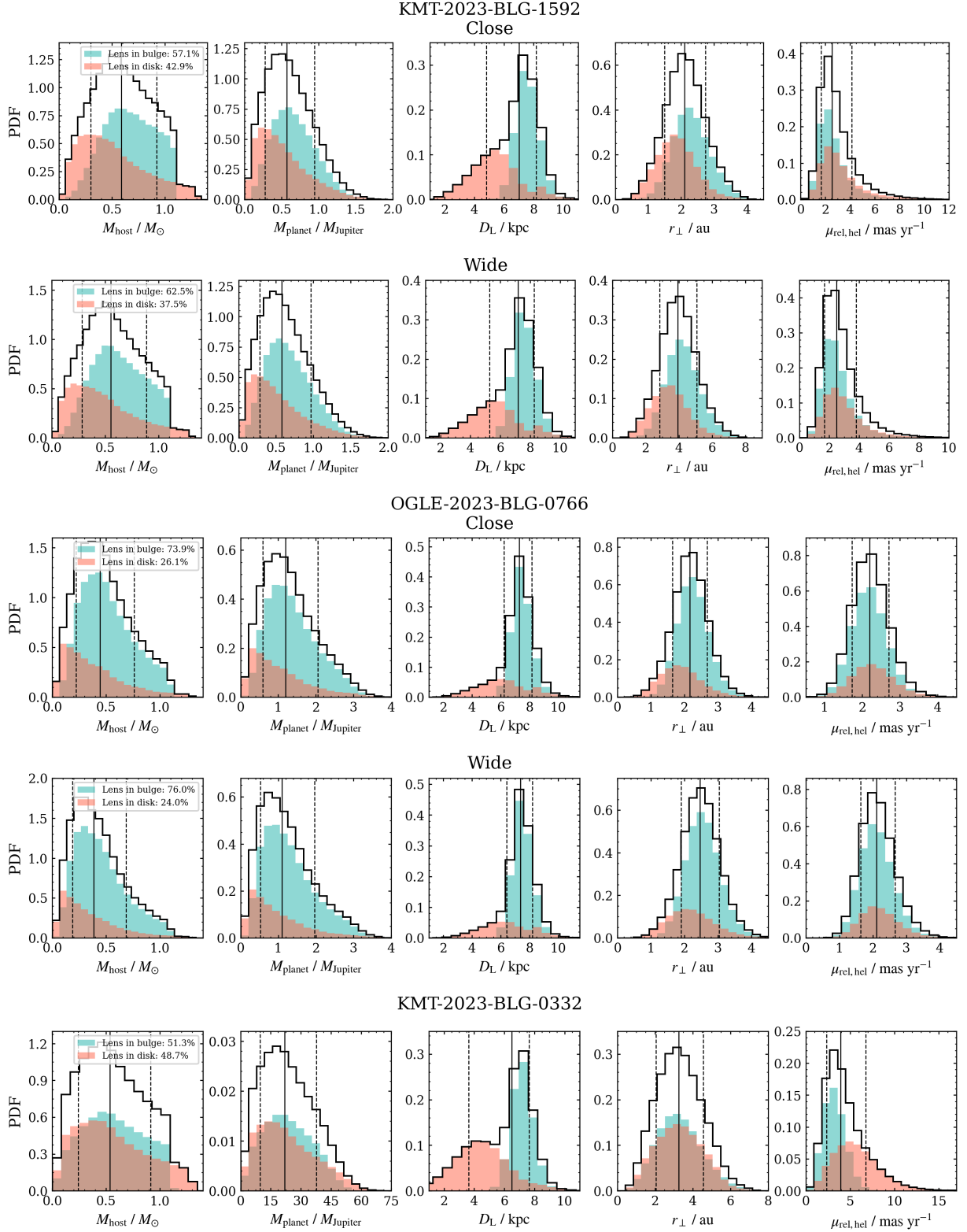


Figure 10. Posterior distributions from the Bayesian analysis for the host mass M_{host} , planetary mass M_{planet} , lens distance D_L , projected planet-host separation r_{\perp} , and the heliocentric lens-source relative proper motion $\mu_{\text{rel, hel}}$. In each panel, the solid black curve denotes the median value, while the dashed black curves represent the 15.9% and 84.1% credible intervals. The contributions from disk and bulge lens populations are illustrated in green and red, respectively.

Z.L., H.L., W.Z., H.Y., Y.T., J.Z. and S.M. acknowledge support by the National Natural Science Foundation of China (Grant No. 12133005). This research has made use of the KMTNet system operated by the Korea Astronomy and Space Science Institute (KASI) at three host sites of CTIO in Chile, SAAO in South Africa, and SSO in Australia. Data transfer from the host site to KASI was supported by the Korea Research Environment Open NETWORK (KREONET). This research was supported by KASI under the R&D program (Project No. 2025-1-830-05) supervised by the Ministry of Science and ICT. The OGLE project has received funding from the Polish National Science Centre grant OPUS 2024/55/B/ST9/00447 awarded to A.U. The MOA project is supported by JSPS KAKENHI Grant Number JP24253004,

JP26247023, JP16H06287 and JP22H00153. This work is part of the ET space mission which is funded by the China's Space Origins Exploration Program. H.Y. acknowledges support by the China Postdoctoral Science Foundation (No. 2024M762938). Y.S. acknowledges support from BSF Grant No. 2020740. R.P. acknowledges support by the Polish National Agency for Academic Exchange grant "Polish Returns 2019."

Software: pySIS (Albrow et al. 2009; Yang et al. 2024, 2025), numpy (Harris et al. 2020), emcee (Goodman & Weare 2010; Foreman-Mackey et al. 2013), Matplotlib (Hunter 2007), SciPy (Virtanen et al. 2020), VBBL Bozza (2010); Bozza et al. (2018, 2025)

REFERENCES

- Adams, A. D., Boyajian, T. S., & von Braun, K. 2018, MNRAS, 473, 3608, doi: [10.1093/mnras/stx2367](https://doi.org/10.1093/mnras/stx2367)
- Alard, C., & Lupton, R. H. 1998, ApJ, 503, 325, doi: [10.1086/305984](https://doi.org/10.1086/305984)
- Albrow, M. D., Horne, K., Bramich, D. M., et al. 2009, MNRAS, 397, 2099, doi: [10.1111/j.1365-2966.2009.15098.x](https://doi.org/10.1111/j.1365-2966.2009.15098.x)
- Batista, V., Gould, A., Dieters, S., et al. 2011, A&A, 529, A102, doi: [10.1051/0004-6361/201016111](https://doi.org/10.1051/0004-6361/201016111)
- Bennett, D. P., Bond, I. A., Udalski, A., et al. 2008, ApJ, 684, 663, doi: [10.1086/589940](https://doi.org/10.1086/589940)
- Bensby, T., Yee, J. C., Feltzing, S., et al. 2013, A&A, 549, A147, doi: [10.1051/0004-6361/201220678](https://doi.org/10.1051/0004-6361/201220678)
- Blackman, J. W., Beaulieu, J. P., Bennett, D. P., et al. 2021, Nature, 598, 272, doi: [10.1038/s41586-021-03869-6](https://doi.org/10.1038/s41586-021-03869-6)
- Bond, I. A., Abe, F., Dodd, R. J., et al. 2001, MNRAS, 327, 868, doi: [10.1046/j.1365-8711.2001.04776.x](https://doi.org/10.1046/j.1365-8711.2001.04776.x)
- Bozza, V. 2010, MNRAS, 408, 2188, doi: [10.1111/j.1365-2966.2010.17265.x](https://doi.org/10.1111/j.1365-2966.2010.17265.x)
- Bozza, V., Bachelet, E., Bartolčić, F., et al. 2018, MNRAS, 479, 5157, doi: [10.1093/mnras/sty1791](https://doi.org/10.1093/mnras/sty1791)
- Bozza, V., Saggese, V., Covone, G., Rota, P., & Zhang, J. 2025, A&A, 694, A219, doi: [10.1051/0004-6361/202452648](https://doi.org/10.1051/0004-6361/202452648)
- Cassan, A., Kubas, D., Beaulieu, J. P., et al. 2012, Nature, 481, 167, doi: [10.1038/nature10684](https://doi.org/10.1038/nature10684)
- Dong, S., DePoy, D. L., Gaudi, B. S., et al. 2006, ApJ, 642, 842, doi: [10.1086/501224](https://doi.org/10.1086/501224)
- Foreman-Mackey, D., Hogg, D. W., Lang, D., & Goodman, J. 2013, PASP, 125, 306, doi: [10.1086/670067](https://doi.org/10.1086/670067)
- Gaudi, B. S. 1998, ApJ, 506, 533, doi: [10.1086/306256](https://doi.org/10.1086/306256)
- Ge, J., Zhang, H., Zang, W., et al. 2022, arXiv e-prints, arXiv:2206.06693. <https://arxiv.org/abs/2206.06693>
- Goodman, J., & Weare, J. 2010, Communications in Applied Mathematics and Computational Science, 5, 65, doi: [10.2140/camcos.2010.5.65](https://doi.org/10.2140/camcos.2010.5.65)
- Gould, A. 1992, ApJ, 392, 442, doi: [10.1086/171443](https://doi.org/10.1086/171443)
- . 1994, ApJL, 421, L75, doi: [10.1086/187191](https://doi.org/10.1086/187191)
- . 2000, ApJ, 542, 785, doi: [10.1086/317037](https://doi.org/10.1086/317037)
- . 2004, ApJ, 606, 319, doi: [10.1086/382782](https://doi.org/10.1086/382782)
- . 2022, arXiv e-prints, arXiv:2209.12501. <https://arxiv.org/abs/2209.12501>
- Gould, A., & Loeb, A. 1992, ApJ, 396, 104, doi: [10.1086/171700](https://doi.org/10.1086/171700)
- Gould, A., Zang, W.-C., Mao, S., & Dong, S.-B. 2021, Research in Astronomy and Astrophysics, 21, 133, doi: [10.1088/1674-4527/21/6/133](https://doi.org/10.1088/1674-4527/21/6/133)
- Gould, A., Udalski, A., Monard, B., et al. 2009, ApJL, 698, L147, doi: [10.1088/0004-637X/698/2/L147](https://doi.org/10.1088/0004-637X/698/2/L147)
- Gould, A., Dong, S., Gaudi, B. S., et al. 2010, ApJ, 720, 1073, doi: [10.1088/0004-637X/720/2/1073](https://doi.org/10.1088/0004-637X/720/2/1073)
- Gould, A., Jung, Y. K., Hwang, K.-H., et al. 2022a, Journal of Korean Astronomical Society, 55, 173, doi: [10.5303/JKAS.2022.55.5.173](https://doi.org/10.5303/JKAS.2022.55.5.173)
- Gould, A., Han, C., Zang, W., et al. 2022b, A&A, 664, A13, doi: [10.1051/0004-6361/202243744](https://doi.org/10.1051/0004-6361/202243744)
- Griest, K., & Safizadeh, N. 1998, ApJ, 500, 37, doi: [10.1086/305729](https://doi.org/10.1086/305729)
- Gui, Y., Zang, W., Zhai, R., et al. 2024, AJ, 168, 49, doi: [10.3847/1538-3881/ad4ce5](https://doi.org/10.3847/1538-3881/ad4ce5)
- Han, C., Jung, Y. K., Udalski, A., et al. 2013, ApJ, 778, 38, doi: [10.1088/0004-637X/778/1/38](https://doi.org/10.1088/0004-637X/778/1/38)
- Han, C., Lee, C.-U., Udalski, A., et al. 2020, AJ, 159, 134, doi: [10.3847/1538-3881/ab6f66](https://doi.org/10.3847/1538-3881/ab6f66)
- Han, C., Ryu, Y.-H., Shin, I.-G., et al. 2022, A&A, 667, A64, doi: [10.1051/0004-6361/202244186](https://doi.org/10.1051/0004-6361/202244186)
- Han, C., Kil Jung, Y., Kim, D., et al. 2023a, A&A, 675, A71, doi: [10.1051/0004-6361/202245455](https://doi.org/10.1051/0004-6361/202245455)
- Han, C., Jung, Y. K., Bond, I. A., et al. 2023b, A&A, 678, A190, doi: [10.1051/0004-6361/202347014](https://doi.org/10.1051/0004-6361/202347014)

- Han, C., Bond, I. A., Udalski, A., et al. 2024a, *A&A*, 687, A241, doi: [10.1051/0004-6361/202449618](https://doi.org/10.1051/0004-6361/202449618)
- Han, C., Udalski, A., Lee, C.-U., et al. 2024b, *A&A*, 683, A187, doi: [10.1051/0004-6361/202348245](https://doi.org/10.1051/0004-6361/202348245)
- Han, C., Bond, I. A., Udalski, A., et al. 2024c, *A&A*, 691, A237, doi: [10.1051/0004-6361/202451416](https://doi.org/10.1051/0004-6361/202451416)
- Han, C., Bond, I. A., Jung, Y. K., et al. 2025, *A&A*, 694, A90, doi: [10.1051/0004-6361/202452027](https://doi.org/10.1051/0004-6361/202452027)
- Harris, C. R., Millman, K. J., van der Walt, S. J., et al. 2020, *Nature*, 585, 357, doi: [10.1038/s41586-020-2649-2](https://doi.org/10.1038/s41586-020-2649-2)
- Holtzman, J. A., Watson, A. M., Baum, W. A., et al. 1998, *AJ*, 115, 1946, doi: [10.1086/300336](https://doi.org/10.1086/300336)
- Hunter, J. D. 2007, *Computing in Science & Engineering*, 9, 90, doi: [10.1109/MCSE.2007.55](https://doi.org/10.1109/MCSE.2007.55)
- Hwang, K.-H., Choi, J.-Y., Bond, I. A., et al. 2013, *ApJ*, 778, 55, doi: [10.1088/0004-637X/778/1/55](https://doi.org/10.1088/0004-637X/778/1/55)
- Ida, S., & Lin, D. N. C. 2004, *ApJ*, 604, 388, doi: [10.1086/381724](https://doi.org/10.1086/381724)
- Jiang, G., DePoy, D. L., Gal-Yam, A., et al. 2004, *ApJ*, 617, 1307, doi: [10.1086/425678](https://doi.org/10.1086/425678)
- Jung, Y. K., Zang, W., Han, C., et al. 2022, *AJ*, 164, 262, doi: [10.3847/1538-3881/ac9c5c](https://doi.org/10.3847/1538-3881/ac9c5c)
- Jung, Y. K., Zang, W., Wang, H., et al. 2023, *AJ*, 165, 226, doi: [10.3847/1538-3881/accb8f](https://doi.org/10.3847/1538-3881/accb8f)
- Kennedy, G. M., & Kenyon, S. J. 2008, *ApJ*, 673, 502, doi: [10.1086/524130](https://doi.org/10.1086/524130)
- Kim, D.-J., Kim, H.-W., Hwang, K.-H., et al. 2018a, *AJ*, 155, 76, doi: [10.3847/1538-3881/aaa47b](https://doi.org/10.3847/1538-3881/aaa47b)
- Kim, H.-W., Hwang, K.-H., Shvartzvald, Y., et al. 2018b, arXiv e-prints, arXiv:1806.07545. <https://arxiv.org/abs/1806.07545>
- Kim, S.-L., Lee, C.-U., Park, B.-G., et al. 2016, *Journal of Korean Astronomical Society*, 49, 37, doi: [10.5303/JKAS.2016.49.1.37](https://doi.org/10.5303/JKAS.2016.49.1.37)
- Mao, S., & Paczynski, B. 1991, *ApJL*, 374, L37, doi: [10.1086/186066](https://doi.org/10.1086/186066)
- Mordasini, C., Alibert, Y., & Benz, W. 2009, *A&A*, 501, 1139, doi: [10.1051/0004-6361/200810301](https://doi.org/10.1051/0004-6361/200810301)
- Mróz, P., A., Skowron, J., et al. 2017, *Nature*, 548, 183, doi: [10.1038/nature23276](https://doi.org/10.1038/nature23276)
- Nataf, D. M., Gould, A., Fouqué, P., et al. 2013, *ApJ*, 769, 88, doi: [10.1088/0004-637X/769/2/88](https://doi.org/10.1088/0004-637X/769/2/88)
- Nemiroff, R. J., & Wickramasinghe, W. A. D. T. 1994, *ApJL*, 424, L21, doi: [10.1086/187265](https://doi.org/10.1086/187265)
- Paczynski, B. 1986, *ApJ*, 304, 1, doi: [10.1086/164140](https://doi.org/10.1086/164140)
- Penny, M. T., Gaudi, B. S., Kerins, E., et al. 2019, *ApJS*, 241, 3, doi: [10.3847/1538-4365/aafb69](https://doi.org/10.3847/1538-4365/aafb69)
- Penny, M. T., Henderson, C. B., & Clanton, C. 2016, *ApJ*, 830, 150, doi: [10.3847/0004-637X/830/2/150](https://doi.org/10.3847/0004-637X/830/2/150)
- Poindexter, S., Afonso, C., Bennett, D. P., et al. 2005, *ApJ*, 633, 914, doi: [10.1086/468182](https://doi.org/10.1086/468182)
- Poleski, R., Skowron, J., Mróz, P., et al. 2021, *AcA*, 71, 1, doi: [10.32023/0001-5237/71.1.1](https://doi.org/10.32023/0001-5237/71.1.1)
- Ryu, Y.-H., Yee, J. C., Udalski, A., et al. 2018, *AJ*, 155, 40, doi: [10.3847/1538-3881/aa9be4](https://doi.org/10.3847/1538-3881/aa9be4)
- Sako, T., Sekiguchi, T., Sasaki, M., et al. 2008, *Experimental Astronomy*, 22, 51, doi: [10.1007/s10686-007-9082-5](https://doi.org/10.1007/s10686-007-9082-5)
- Shin, I. G., Yee, J. C., Gould, A., et al. 2019, *AJ*, 158, 199, doi: [10.3847/1538-3881/ab46a5](https://doi.org/10.3847/1538-3881/ab46a5)
- Shin, I.-G., Yee, J. C., Zang, W., et al. 2023, *AJ*, 166, 104, doi: [10.3847/1538-3881/ace96d](https://doi.org/10.3847/1538-3881/ace96d)
- Shvartzvald, Y., Maoz, D., Udalski, A., et al. 2016, *MNRAS*, 457, 4089, doi: [10.1093/mnras/stw191](https://doi.org/10.1093/mnras/stw191)
- Skowron, J., Udalski, A., Gould, A., et al. 2011, *ApJ*, 738, 87, doi: [10.1088/0004-637X/738/1/87](https://doi.org/10.1088/0004-637X/738/1/87)
- Sumi, T., Kamiya, K., Bennett, D. P., et al. 2011, *Nature*, 473, 349, doi: [10.1038/nature10092](https://doi.org/10.1038/nature10092)
- Sumi, T., Koshimoto, N., Bennett, D. P., et al. 2023, *AJ*, 166, 108, doi: [10.3847/1538-3881/ace688](https://doi.org/10.3847/1538-3881/ace688)
- Suzuki, D., Bennett, D. P., Sumi, T., et al. 2016, *ApJ*, 833, 145, doi: [10.3847/1538-4357/833/2/145](https://doi.org/10.3847/1538-4357/833/2/145)
- Szymański, M. K., Udalski, A., Soszyński, I., et al. 2011, *AcA*, 61, 83. <https://arxiv.org/abs/1107.4008>
- Tomaney, A. B., & Crotts, A. P. S. 1996, *AJ*, 112, 2872, doi: [10.1086/118228](https://doi.org/10.1086/118228)
- Udalski, A. 2003, *AcA*, 53, 291
- Udalski, A., Szymanski, M., Kaluzny, J., et al. 1994, *AcA*, 44, 227
- Udalski, A., Szymański, M. K., & Szymański, G. 2015, *AcA*, 65, 1. <https://arxiv.org/abs/1504.05966>
- Virtanen, P., Gommers, R., Oliphant, T. E., et al. 2020, *Nature Methods*, 17, 261, doi: [10.1038/s41592-019-0686-2](https://doi.org/10.1038/s41592-019-0686-2)
- Witt, H. J., & Mao, S. 1994, *ApJ*, 430, 505, doi: [10.1086/174426](https://doi.org/10.1086/174426)
- Wozniak, P. R. 2000, *AcA*, 50, 421
- Yang, H., Mao, S., Zang, W., & Zhang, X. 2021, *MNRAS*, 502, 5631, doi: [10.1093/mnras/stab441](https://doi.org/10.1093/mnras/stab441)
- Yang, H., Yee, J. C., Hwang, K.-H., et al. 2024, *MNRAS*, 528, 11, doi: [10.1093/mnras/stad3672](https://doi.org/10.1093/mnras/stad3672)
- Yang, H., Yee, J. C., Zhang, J., et al. 2025, *AJ*, 169, 295, doi: [10.3847/1538-3881/adc73e](https://doi.org/10.3847/1538-3881/adc73e)
- Yee, J. C., Udalski, A., Sumi, T., et al. 2009, *ApJ*, 703, 2082, doi: [10.1088/0004-637X/703/2/2082](https://doi.org/10.1088/0004-637X/703/2/2082)
- Yee, J. C., Shvartzvald, Y., Gal-Yam, A., et al. 2012, *ApJ*, 755, 102, doi: [10.1088/0004-637X/755/2/102](https://doi.org/10.1088/0004-637X/755/2/102)
- Yoo, J., DePoy, D. L., Gal-Yam, A., et al. 2004, *ApJ*, 603, 139, doi: [10.1086/381241](https://doi.org/10.1086/381241)
- Zang, W., Hwang, K.-H., Udalski, A., et al. 2021a, *AJ*, 162, 163, doi: [10.3847/1538-3881/ac12d4](https://doi.org/10.3847/1538-3881/ac12d4)
- Zang, W., Han, C., Kondo, I., et al. 2021b, *Research in Astronomy and Astrophysics*, 21, 239, doi: [10.1088/1674-4527/21/9/239](https://doi.org/10.1088/1674-4527/21/9/239)
- Zang, W., Yang, H., Han, C., et al. 2022, *MNRAS*, 515, 928, doi: [10.1093/mnras/stac1883](https://doi.org/10.1093/mnras/stac1883)
- Zang, W., Jung, Y. K., Yang, H., et al. 2023, *AJ*, 165, 103, doi: [10.3847/1538-3881/acb34b](https://doi.org/10.3847/1538-3881/acb34b)

- Zang, W., Jung, Y. K., Yee, J. C., et al. 2025, *Science*, 388, 400,
doi: [10.1126/science.adn6088](https://doi.org/10.1126/science.adn6088)
- Zhang, K., Zang, W., El-Badry, K., et al. 2024, *Nature Astronomy*,
8, 1575, doi: [10.1038/s41550-024-02375-9](https://doi.org/10.1038/s41550-024-02375-9)